Earth and Planetary Science Letters 454 (2016) 65–77

Contents lists available at ScienceDirect

Earth and Planetary Science Letters

www.elsevier.com/locate/epsl

H_2O-driven generation of picritic melts in the Middle to Late Triassic Stuhini arc of the Stikine terrane, British Columbia, Canada

Dejan Milidragovic [a,*], John B. Chapman [a], Sebastian Bichlmaier [b], Dante Canil [b], Alex Zagorevski [c]

[a] Geological Survey of Canada, 1500-605 Robson Street, Vancouver, BC, V6B 5J3, Canada
[b] School of Earth and Ocean Sciences, University of Victoria, 3800 Finnerty Road, Victoria, BC, V8P 5C2, Canada
[c] Geological Survey of Canada, 601 Booth Street, Ottawa, ON, K1A 0E8, Canada

ARTICLE INFO

Article history:
Received 6 June 2016
Received in revised form 24 August 2016
Accepted 26 August 2016
Available online xxxx
Editor: M. Bickle

Keywords:
arc picrite
Triassic
Stikinia
subduction zone

ABSTRACT

Basaltic to andesitic compositions predominate island arc magmatism; ultramafic magmas are rare. Ultramafic (MgO = 21–33 wt.%) tuff breccia, lapilli tuff, and ash tuff of the Middle to Upper Triassic Stuhini Group were erupted in the Stikine arc of the North American Cordillera shortly preceding an episode of prolific porphyry Cu–Mo(–Au) mineralization. The ultramafic tuff shows accumulation (20–65%) of olivine (Fo_{91}) and minor chromite into a subalkaline picritic parental magma with MgO ~16 wt.%. Despite the inferred high MgO content of the parental liquid, chromite phenocrysts record relatively low liquidus temperatures (<1200 °C) suggesting crystallization from relatively low temperature, hydrous melts, at oxygen fugacities one to three log units above the fayalite–magnetite–quartz (FMQ) buffer. The primary picritic magmas likely contained 5–7 wt.% H_2O, inferred on the basis of olivine-liquid thermometry and thermal models for subduction zones, thus alleviating the need for catastrophic thermal perturbations in the mantle wedge. Instead, efficient release of water through slab dehydration at 2.5–3.0 GPa allows generation of picritic melts at ordinary mantle wedge temperatures through moderate degrees ($F = 0.10$–0.15) of hydrous flux melting. The volatile-rich nature of the melt and the predominant extensional regime in the overlying lithosphere of Stikinia facilitated the near-adiabatic ascent of the Stuhini Group picrites. The high H_2O content of the rapidly ascending picrite melt may have played a key role in transport of metals into the crust of the Stikinia and subsequent porphyry mineralization.

1. Introduction

Primitive, mantle-derived magmas with picritic (MgO >12 wt.%) compositions are uncommon in recent arc settings, but have been identified in the central Aleutian (Nye and Reid, 1986), Japan (Yamamoto, 1988); Vanuatu (Eggins, 1993), Solomon Islands (Rohrbach et al., 2005), and Lesser Antilles arcs (Woodland et al., 2002), and inferred from the Mariana arc (Kelley et al., 2010; Tamura et al., 2011) Paleozoic and Mesozoic arc-related picrites are equally rare, but have been described in eastern Kamchatka (Kamenetsky et al., 1995), the northern Appalachian Orogen (Wilson, 2003), and the Quesnel (Russell and Snyder, 1997) and Stikine (Logan et al., 2000; Logan and Mihalynuk, 2014) arc terranes of the North American Cordillera. The genesis of these highly primitive magmas in arc environments remains poorly understood, in part due to their scarcity. Existing models for petrogenesis of arc picrites commonly invoke unusual or catastrophic geodynamic scenarios, such as ridge subduction, slab tear, assimilation of peridotite, or rapid mantle-wedge counter flow (Nye and Reid, 1986; Rohrbach et al., 2005; Logan and Mihalynuk, 2014).

Picritic rocks in the Stikine terrane comprise a variably serpentinized, olivine-rich pyroclastic unit composed of lapilli breccia, lapilli tuff, and ash tuff (Logan et al., 2000; Milidragovic et al., 2016). The ultramafic pyroclastic rocks form a volumetrically minor component of the Stuhini Group, a predominantly subaqueous volcano-sedimentary arc assemblage of Middle to Late Triassic age. Stuhini arc volcanism was accompanied by a pulse of prolific Late Triassic porphyry Cu–Mo(–Au) mineralization (Logan and Mihalynuk, 2014). Widespread recognition that large porphyry deposits form in response to tectonic and thermal perturbations in the underlying mantle wedge (e.g. Cooke et al., 2005; Logan and Mihalynuk, 2014), requires a closer examination of the spatially and temporarily associated ultramafic rocks. In this paper, we demonstrate that the picritic rocks of the Stikine terrane are hydrous,

* Corresponding author.
E-mail address: dejan.milidragovic604@gmail.com (D. Milidragovic).

http://dx.doi.org/10.1016/j.epsl.2016.08.034
0012-821X/

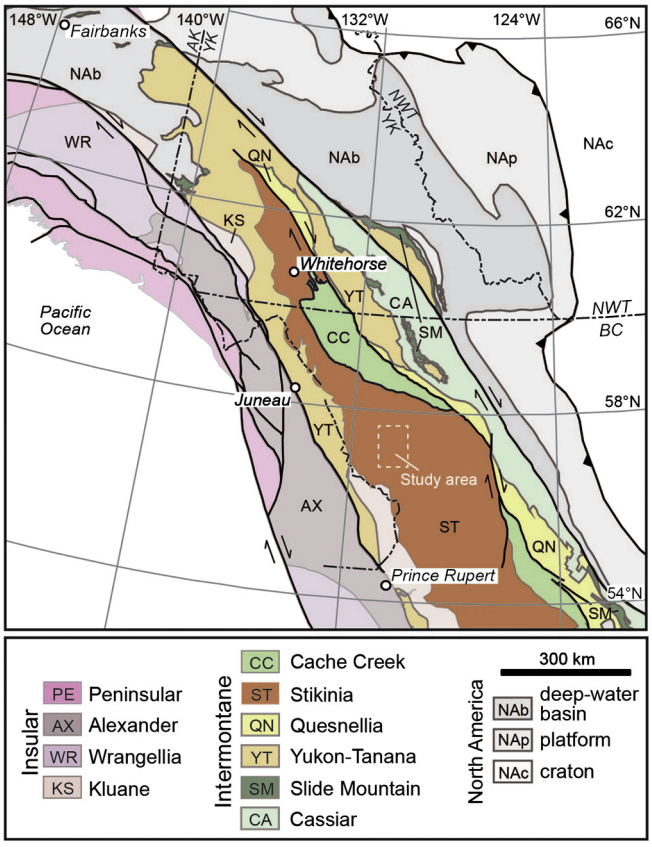

Fig. 1. Terranes of the Canadian Cordillera and the location of Middle to Upper Triassic ultramafic pyroclastic rocks (modified from Nelson et al., 2013).

moderate-degree melts ($F = 0.10$–0.15) of the underlying, depleted arc mantle wedge. We argue that the ultramafic character of the Stuhini Group picrites does not require catastrophic changes to the mantle wedge configuration. Instead we argue that efficient dehydration of the subducting Panthalassan plate is the key in the generation and near-adiabatic ascent of the picritic magmas of the Stuhini Group.

2. The Stikine arc

The Stikine terrane (Fig. 1) of the North American Cordillera preserves a history of island arc magmatism, sedimentation, and deformation spanning from Middle Devonian to Middle Jurassic (Logan et al., 2000; Nelson et al., 2013). One current model (Nelson et al., 2013 and references therein) posits that the Stikine and related terranes formed on variably attenuated Laurentian continental crust, upon which successive magmatic arcs were built. The earliest of these, initiated during the Late Devonian to Early Permian (Stikine Assemblage; Logan et al., 2000), was followed by magmatic hiatus, tectonic quiescence and development of carbonate slope to shale basin by the Middle Triassic.

A resurgence of late Triassic arc activity in the Stikine terrane resulted in deposition of voluminous basalt and andesite of the Stuhini Group (Mihalynuk et al., 1999; Logan et al., 2000). This phase of arc activity was followed by a brief magmatic hiatus, deposition of carbonates, and deformation. The final phase of arc magmatism occurred during the Latest Triassic to Middle Jurassic (Hazelton Group; Barresi et al., 2015), and was followed by accretion of the Stikine terrane to the Laurentian margin.

2.1. The Stuhini Group

The Stuhini Group of northwestern British Columbia, and the correlative Lewes River (southern Yukon) and Takla (central British Columbia) groups, comprise volcano-sedimentary rocks deposited over a wide area of the Stikine terrane in response to Middle to Late Triassic arc volcanism (Hart, 1997; Mihalynuk et al., 1999; Logan et al., 2000). The duration of Middle to Late Triassic arc magmatism is constrained by Ladinian–Carnian fossils at the base of the Stuhini Group (Logan et al., 2000) and by Late Norian to Rhaetian conodonts within limestone that caps the Stuhini and Lewes River groups (Hart, 1997; Mihalynuk et al., 1999). Intrusive activity, evidenced by the ca. 228–215 Ma Stikine plutonic suite (Logan et al., 2000; Logan and Mihalynuk, 2014; Milidragovic et al., 2016), accompanied volcanism and deposition of the Stuhini Group. The Stuhini Group is $\leq$2 km thick (Logan et al., 2000) and composed predominantly of subaqueous mafic to intermediate augite- and/or plagioclase-phyric volcanic flows of tholeiitic to calc-alkaline affinity, pyroclastics, and related volcaniclastic and epiclastic rocks, including pyroxene and feldspar-rich sedimentary rocks, carbonaceous shale, siltstone, and limestone (Logan et al., 2000; Mihalynuk et al., 1999). Ultramafic pyroclastic rocks constitute a volumetrically minor component of the Stuhini Group and are limited to the basal part of its proximal volcanic facies (Mess Lake facies; Logan et al., 2000).

3. Ultramafic pyroclastic unit of the Stuhini Group

Ultramafic pyroclastics form a grey to green-weathering, $\leq$100 m thick, volumetrically minor unit within the Stuhini Group (Logan et al., 2000; Milidragovic et al., 2016). Although the unit can be traced along strike for up to 5 km, it weathers recessively and appears to have served as a locus for late brittle faulting and veining. Despite pervasive serpentinization, the unit preserves primary igneous and depositional textures both on outcrop and thin-section scales. A ~35 m thick, undeformed section of the pyroclastic unit exposes four fining-upward sequences composed of normally-graded tuff breccia and olivine lapilli tuff, capped by beds of rhythmically layered ash tuff (Fig. 2). Layering in ash tuff varies from coarse to fine ($\leq$3 mm to $\geq$5 cm), and is parallel and continuous on outcrop scale. The base of each fining upward sequence is sharp and locally marked by low-amplitude scouring of underlying ash tuff beds (Milidragovic et al., 2016).

The primary mineralogy of the ultramafic rocks has been largely replaced by serpentine, magnetite, talc, tremolite, and chlorite. Primary minerals comprise sparse relict olivine, and chromite mantled by late/metamorphic magnetite. The euhedral to subhedral shape of pseudomorphed olivine and chromite grains suggests they are cognate crystals from a primitive parental magma, rather than xenocrysts acquired during magma ascent and explosive eruption. The frequent inclusion of euhedral chromite crystals in pseudomorphed olivine (Fig. B1–1F) indicates that the two minerals co-crystallized as high-temperature liquidus phases. Rare clinopyroxene also occurs as euhedral to subhedral grains that typically form clusters and may be xenocrysts entrained during magma ascent. Plagioclase is entirely absent. Similarly, non-cognate lithic clasts are sparse. Bomb and lapilli-sized fragments are vesicular and contain abundant dark, euhedral to subhedral serpentine pseudomorphs (lizardite partially overprinted by antigorite and talc), magnetite, trace calcite, and rare chromite phenocrysts. Late calcite rarely replaces serpentine and is often spatially associated with mm-scale veinlets. Pseudomorphed olivine and chromite phenocrysts are hosted in a fine-grained, commonly frothy, devitrified groundmass composed of very fine-grained chlorite and clay. Scoriaceous lapilli, entirely composed of vesicular, devitrified glass are less common, although intense serpentine and chlorite alteration and overprinting of primary pyroclastic textures may, in part, account for this apparent scarcity. Very fine-grained, pale green tremolite crystals often occur as randomly oriented mats overprinting earlier alteration. The lapilli and bomb-sized fragments

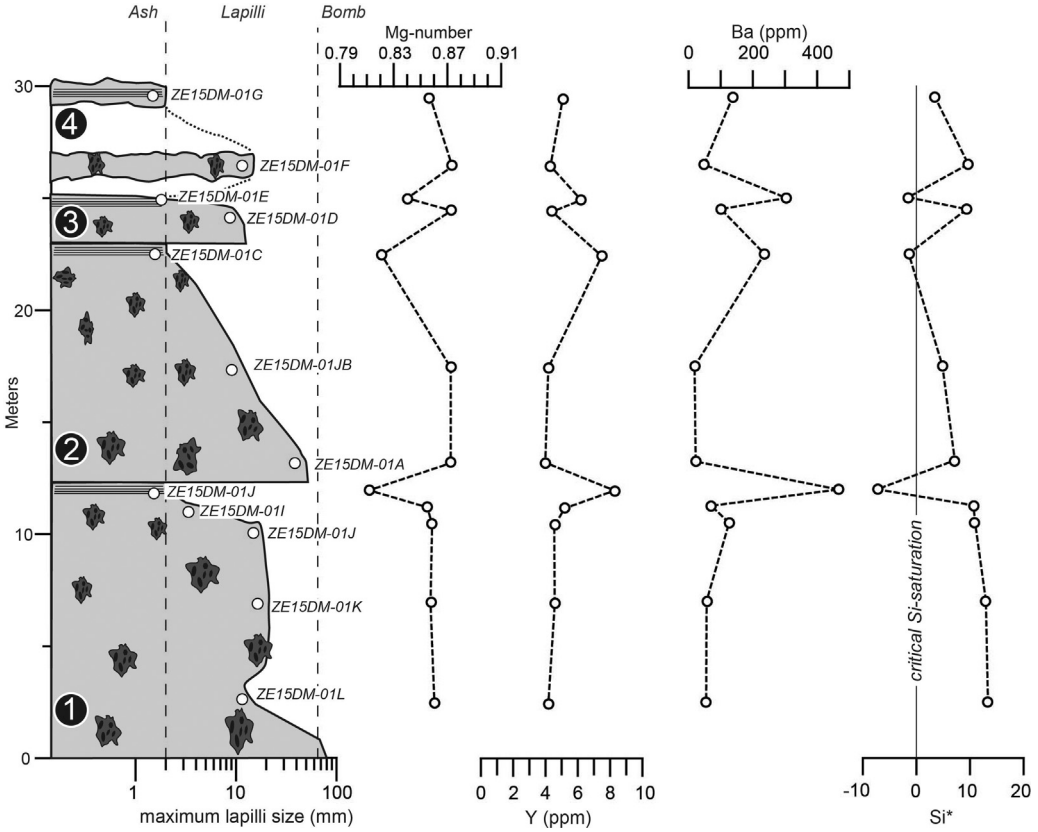

Fig. 2. Schematic section through the ultramafic pyroclastic unit, showing sampled locations and key geochemical indices (Mg-number, Y, Ba, and Si*). Si*, the index of Si-saturation, is calculated from the normative mineralogy calculated in oxygen units using $Si^* = Qz_n + 1/3Hy_n - Lc_n - Ne_n$, where Qz_n, Hy_n, Lc_n, and Ne_n are normative quartz, hypersthene, leucite, and nepheline, respectively.

are supported in a matrix of serpentinized olivine, chlorite, and devitrified glass. Ash tuff beds are predominantly composed of serpentinized olivine fragments and devitrified shards of glass, some of which display cuspate bubble-wall morphologies (achneliths; cf. Walker and Croasdale, 1972) and indicate rapid cooling. Glass shards have been replaced completely by penninite (chlorite) and palagonite. The macroscopic layering observed in outcrop is a manifestation of variation in the abundance of olivine and devitrified glass.

4. Analytical methods

Thirty five samples of ultramafic tuff were analyzed at Activation Laboratories (Ancaster, ON) for whole-rock major and trace element compositions (Table 1; Electronic Appendix Table A1). Care was taken to select samples that were free of obvious fractures and non-cognate lithic clasts. Pulverized samples were mixed with a flux of lithium metaborate/tetraborate, fused, and dissolved in nitric acid. The concentrations of major elements, and select trace elements (Sc, V, Be, Ba, Sr, and Zr) were measured by inductively coupled plasma-optical emission spectrometry (ICP-OES). The remaining trace elements, including REE, were determined by inductively coupled plasma-mass spectrometry (ICP-MS).

The uncertainty in measurement, at a 95% confidence interval, is $\leq$6% relative for most major elements (Electronic Appendix Table A2). Due to low concentrations, the relative uncertainty in the measurement of Na_2O, K_2O, and P_2O_5 is larger; near the quantification limit (defined as 3.33 times the detection limit) the relative uncertainty is $\sim$30% for Na_2O and P_2O_5 and $\sim$50% for K_2O. The relative uncertainty in most trace element concentrations varies between $<$5% (Cr, Ni) to $\leq$40% (Nb, Ta, Hf) at a 95% confidence level. The relative uncertainty in concentration of rare earth elements (REE), Y, Zr, Th, and U is $\leq$25%, whereas the relative uncertainty in the measurement of large ion lithophile elements (LILE) varies from $\sim$5% (Sr) to $\leq$40% (Ba).

Compositions of olivine and chromite phenocrysts were measured at the University of British Columbia on a Cameca SX50 electron microprobe (Electronic Appendix tables A3 to A5). Analyses by wavelength dispersive spectrometry (WDS) were performed using 20 kV accelerating voltage, 15 nA beam current, and 5 µm beam diameter. Errors in SiO_2 and MgO measurements on olivine are $<$1% relative (2 S.D.), whereas the uncertainty in FeO measurement is $\leq$3% relative. The relative uncertainty in minor oxide constituents of olivine (NiO, MnO) is typically $<$50%. The concentrations of TiO_2, Al_2O_3, Cr_2O_3, and CaO in olivine are near or below detection limit. Errors on major oxide measurements in chromite (Cr_2O_3, Al_2O_3, FeO, MgO) are $\leq$3.5% relative at a 95% confidence interval, whereas the uncertainty in measurement of minor constituents ($\leq$1 wt.%; TiO_2, NiO) may exceed 70%. The concentrations of Si, Ca, Mn, Nb, Ta, and V are typically below detection limit.

5. Results

5.1. Whole rock chemistry

The ultramafic pyroclastic rocks have high loss on ignition (LOI) values (4–14 wt.%), high MgO concentrations (22–37 wt.% LOI-free), and relatively low abundance of all other major elements, consistent with their serpentine-dominated mineralogy. Immobile elements (Al_2O_3, TiO_2, and P_2O_5) and CaO are negatively correlated with MgO (Fig. 3A), whereas SiO_2, Na_2O, and K_2O show no strong dependence on MgO (Fig. 3B). Overall, ash tuff is characterized by lower concentrations of MgO than the coarser grained lapilli tuff and tuff breccia. Nickel (700–1400 ppm) is strongly and positively

Table 1
Major and trace element compositions of representative ultramafic pyroclastics of the Stuhini Group.

Sample #	ZE15DM-01A	ZE15DM-01B	ZE15DM-01C	ZE15DM-01F	ZE15DM-01G	ZE15DM3-01A	ZE15DM3-02D	ZE15DM3-02E	ZE15DM3-02F	ZE15DM5-03A	ZE15DM5-04A	ZE15DM5-07B	ZE15DM7-02B
Easting	381566	381566	381566	381566	381566	381904	382025	382025	382032	359742	359661	359312	360027
Northing	6347445	6347445	6347445	6347445	6347445	6348698	6348597	6348597	6348591	6378259	6378165	6378727	6341500
Lithology	lapilli tuff	lapilli tuff	ash tuff	lapilli tuff	ash tuff	lapilli tuff	ash tuff	ash tuff	lapilli tuff	lapilli tuff	lapilli tuff	lapilli tuff	lapilli tuff
Major elements (wt.%)													
SiO_2	38.77	39.50	40.70	39.76	40.60	40.18	42.43	41.31	39.05	40.79	42.83	41.80	41.52
TiO_2	0.22	0.21	0.38	0.22	0.25	0.24	0.43	0.42	0.22	0.24	0.30	0.30	0.24
Al_2O_3	3.97	3.96	6.18	4.07	4.46	3.93	7.13	7.08	3.90	3.99	5.14	5.42	4.44
Fe_2O_3	9.38	9.25	9.82	9.05	9.38	9.25	10.40	10.59	8.99	9.47	10.05	9.52	9.90
MnO	0.13	0.15	0.16	0.14	0.14	0.13	0.16	0.17	0.14	0.14	0.15	0.14	0.14
MgO	32.67	32.32	22.89	31.78	28.46	29.78	21.49	22.77	30.09	30.72	30.34	27.98	31.82
CaO	3.16	4.67	13.37	2.91	7.15	5.77	10.04	8.55	5.73	4.44	5.62	6.24	4.10
K_2O	0.07	0.04	0.12	0.13	0.22	0.05	3.72	3.20	0.11	0.02	0.06	0.04	0.37
Na_2O	0.05	0.15	0.13	0.05	0.14	0.05	0.21	0.19	0.07	0.13	0.38	0.29	0.27
P_2O_5	0.04	0.06	0.10	0.05	0.06	0.06	0.11	0.10	0.05	0.08	0.08	0.10	0.07
LOI	11.74	9.40	6.42	11.73	9.79	10.35	3.85	4.82	10.68	8.71	4.75	8.59	6.52
Total	100.20	99.70	100.30	99.88	100.60	99.78	99.97	99.19	99.02	98.74	99.72	100.40	99.40
Trace elements (ppm)													
Cs	0.6	0.2	0.2	0.6	0.5	0.1	1.7	1.4	0.3	0.2	0.3	0.9	0.3
Rb	4	1	3	5	6	2	54	52	2	< 1	1	3	4
Ba	23	20	236	48	138	107	1255	963	97	8	29	22	176
Th	0.14	0.14	0.24	0.14	0.16	0.14	0.27	0.25	0.14	0.18	0.18	0.23	0.16
U	0.10	0.12	0.19	0.09	0.14	0.12	0.26	0.24	0.13	0.13	0.14	0.17	0.12
Nb	0.5	0.3	0.4	<0.2	<0.2	<0.2	<0.2	<0.2	<0.2	0.4	0.4	0.3	< 0.2
Ta	0.05	0.03	0.05	0.05	0.04	0.04	0.06	0.05	0.04	0.06	0.08	0.06	0.04
Pb	<5	<5	<5	<5	<5	<5	<5	<5	<5	<5	<5	5	<5
Sr	106	49	164	225	320	70	213	197	121	56	114	123	83
Zr	13	12	19	12	13	13	23	22	12	12	15	16	11
Hf	0.3	0.3	0.5	0.3	0.3	0.3	0.5	0.6	0.2	0.3	0.4	0.5	0.3
Y	4.0	4.2	7.5	4.3	5.1	4.7	8.6	8.3	4.3	4.9	5.8	6.3	4.8
Ga	4	4	4	5	4	4	4	5	4	4	5	6	5
Sc	16	16	26	16	19	17	29	29	16	17	19	20	17
V	94	107	168	98	120	109	195	192	97	110	127	136	107
Co	82	84	64	84	76	80	65	67	79	83	82	77	86
Zn	50	50	70	50	60	50	70	60	60	60	60	60	60
Cu	40	30	70	30	50	40	80	70	40	30	60	50	30
Cr	1810	1860	1740	1840	1780	1900	1730	1790	1750	1940	1750	1760	1940
Ni	1260	1280	720	1270	1080	1190	700	740	1140	1200	1140	1050	1270
La	1.20	1.24	2.21	1.30	1.53	1.45	2.57	2.55	1.32	2.80	2.07	2.70	1.68
Ce	2.50	2.55	4.53	2.70	3.25	2.95	5.43	5.45	2.72	4.76	4.23	5.39	3.18
Pr	0.36	0.37	0.71	0.41	0.48	0.38	0.78	0.73	0.36	0.49	0.57	0.67	0.44
Nd	1.82	1.77	3.12	2.07	2.26	2.06	3.64	3.91	1.81	2.48	2.54	3.45	1.96
Sm	0.49	0.6	0.85	0.63	0.71	0.67	1.08	1.13	0.59	0.77	0.72	0.93	0.55
Eu	0.198	0.206	0.335	0.216	0.243	0.224	0.440	0.391	0.241	0.253	0.271	0.370	0.229
Gd	0.58	0.64	1.25	0.73	0.88	0.81	1.45	1.43	0.70	0.92	1.01	1.02	0.87
Tb	0.11	0.12	0.22	0.13	0.15	0.13	0.25	0.24	0.12	0.14	0.17	0.18	0.15
Dy	0.72	0.75	1.38	0.83	0.94	0.82	1.53	1.40	0.74	0.83	1.02	1.03	0.92
Ho	0.14	0.15	0.28	0.16	0.19	0.16	0.30	0.29	0.15	0.16	0.19	0.20	0.18
Er	0.39	0.41	0.81	0.44	0.54	0.45	0.88	0.86	0.42	0.46	0.53	0.57	0.49
Tm	0.058	0.060	0.114	0.068	0.081	0.066	0.127	0.124	0.067	0.069	0.080	0.087	0.070
Yb	0.37	0.40	0.72	0.45	0.53	0.42	0.80	0.80	0.43	0.43	0.52	0.59	0.41
Lu	0.054	0.061	0.113	0.072	0.081	0.064	0.127	0.129	0.064	0.063	0.076	0.092	0.064

UTM coordinates for sample locations are based on Zone 9 North American Datum 1983 (NAD83).

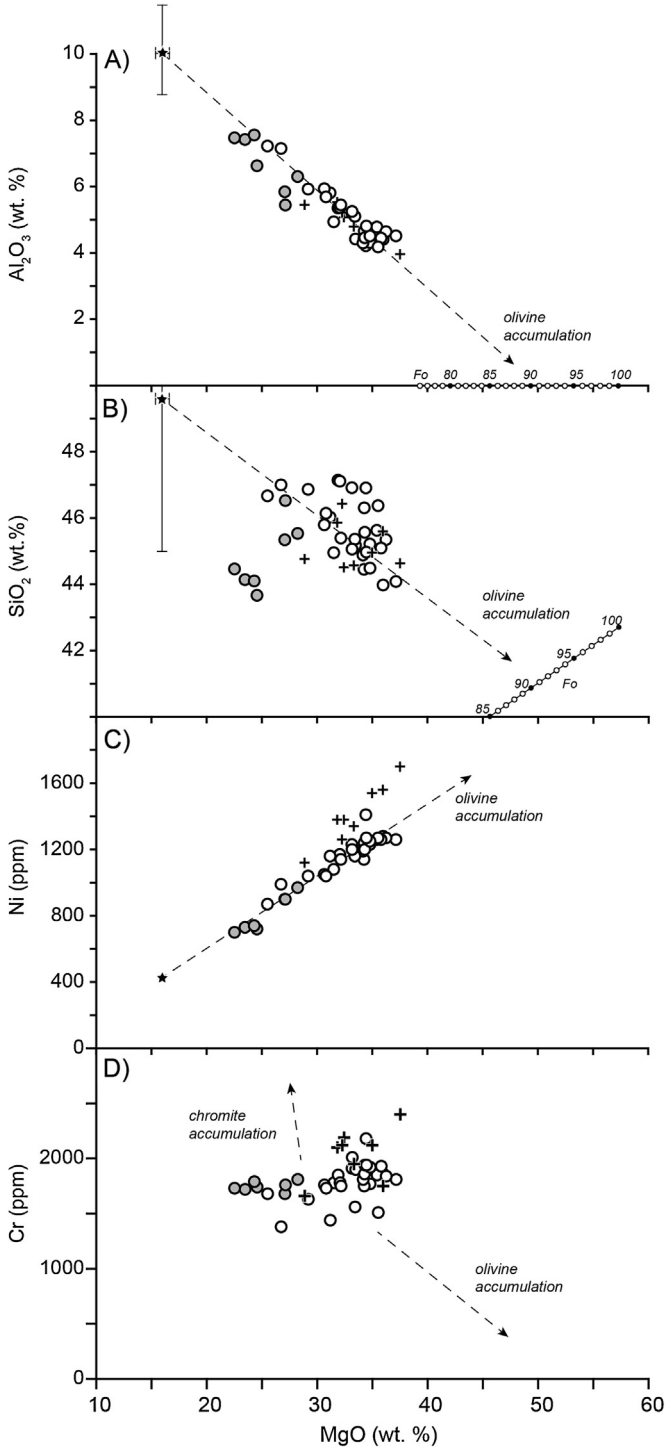

Fig. 3. Major element composition of the Stuhini Group picrites. A) Al_2O_3 (wt.% LOI-free), B) SiO_2, C) Ni (ppm), D) Cr vs. MgO. Circles: data presented in this paper (white: hy-normative, grey: ne-normative); crosses: analyses from Milidragovic et al. (2016). Black star: calculated median parental magma composition with 95th percentile envelope.

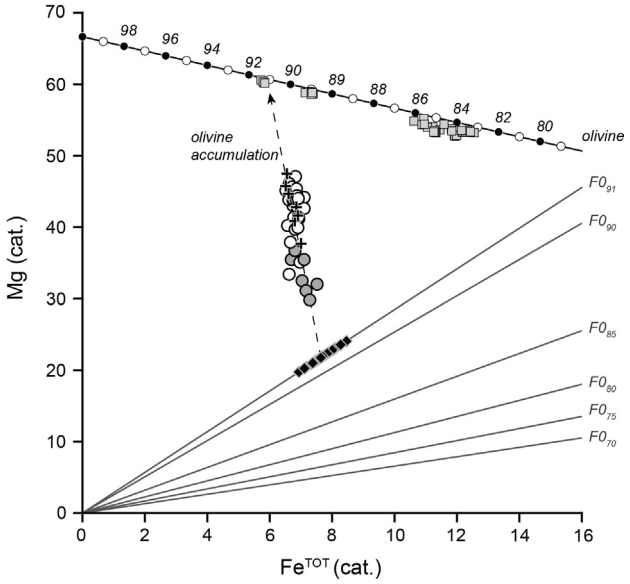

Fig. 4. Mg vs. Fe^{TOT} in cation units (symbols as in Fig. 3; grey squares: WDS olivine analyses). The ultramafic rocks of the Stuhini Group define an olivine control line, which intersects the stoichiometric olivine line at ~Fo_{91}. Lines radiating from the origin are isopleths of olivine composition coexisting with liquids whose Fe and Mg contents are specified by graph coordinates. The isopleths were calculated assuming $K_D = 0.32$ (e.g. Putirka et al., 2011), and $Fe^{3+}/Fe^{TOT} = 0.12$ (see sections 6.2 and 6.3 for discussion of fO_2 and Fe^{3+}/Fe^{TOT} of the parental magma). Black diamonds: parental liquids, in equilibrium with Fo_{91}, calculated by subtraction of olivine from each sample.

correlated with MgO (Fig. 3C), whereas the concentration of Cr (1400–2400) is not correlated with MgO (Fig. 3D). Analyzed rocks display a limited range of FeO^{TOT} concentrations (9.0–10.2 wt.%) that have a weak negative dependence on MgO. On a cation unit plot of Mg vs. Fe^{TOT} samples of the ultramafic tuff form a nearly vertical array that defines an olivine control line (Fig. 4) and intersects the stoichiometric olivine line at ~Fo_{91}. Despite the overall geochemical similarity of the analyzed samples, individual upward-fining sequences show systematic variations in key geochemical indices – a decrease in Mg-number ($Mg/Mg + Fe^{TOT}$) to values <0.85, and an accompanying increase in the abundance of the mobile incompatible elements Na_2O and K_2O are observed in the capping ash tuff beds (Fig. 2). Furthermore, in contrast to tuff breccia and lapilli tuff, which are hypersthene normative (Si-saturated), ash tuff beds are characteristically nepheline-normative (Si-undersaturated).

The absolute abundance of immobile trace elements, especially heavy rare earth elements (HREE), in the ultramafic tuff is significantly less than in mid-ocean ridge basalt (MORB). The absolute trace element abundances are lowest in lapilli tuff and tuff breccia; samples of ash tuff generally exhibit higher abundances of all trace elements (Fig. 5). The ultramafic rocks have primitive mantle (PM)-normalized trace element profiles characterized by relatively unfractionated heavy rare earth elements (HREE), moderate enrichments of light REE (LREE) relative to middle REE (MREE), strong depletions in Nb and Ta relative to LREE, and moderate to strong relative enrichments of large ion lithophile elements (LILE). The relative enrichment of LILE, and to a lesser degree the other less mobile trace elements, is most pronounced in the fine-grained, nepheline-normative samples.

5.2. Mineral chemistry

Olivine is pervasively serpentinized in nearly all samples; relict cores or whole grains are rare. Within individual samples, analyzed olivine displays relatively uniform compositions, exemplified by Fo variability of ≤0.02. Between samples, however, there is considerable compositional variability, most notably in Fo content (0.80–0.91) and concentration of Mn (1,500–17,000 ppm).

Euhedral to subhedral chromite grains are typically inclusion free and mantled by rims of magnetite ('ferritchromit'), likely formed during the serpentinization of the host rock. Within individual samples, chromite is heterogeneous displaying a range of Cr_2O_3 (41–62 wt.%), Al_2O_3 (5.5–15.5 wt.%), and FeO^{TOT} (17–31 wt.%)

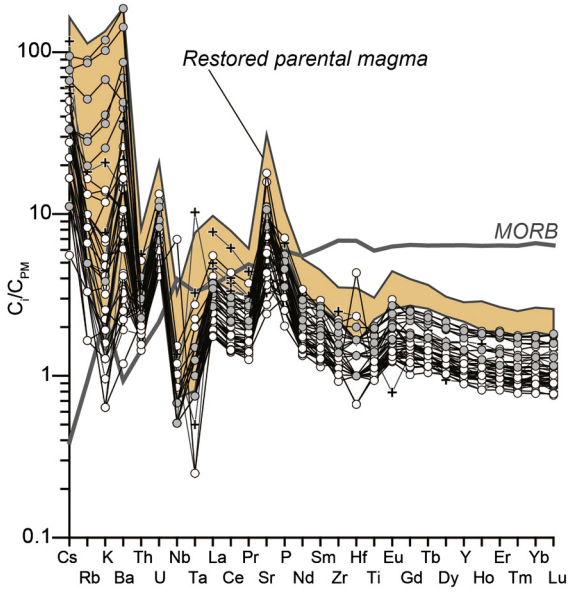

Fig. 5. Primitive mantle-normalized (normalization values after Palme and O'Neill, 2003) trace element profiles of the ultramafic pyroclastic rocks of the Stuhini Group. Symbols as in Fig. 4. Tan field: 95th percentile envelope of the calculated parental picritic magma. The composition of MORB (Sun and McDonough, 1989) is shown for reference.

concentrations. The ratio of ferric to total iron (Fe^{3+}/Fe^{TOT}) in chromite, calculated assuming perfect spinel stoichiometry (XY_2O_4), varies from 0.25 to 0.50 and is positively correlated with Al_2O_3 and TiO_2 and negatively correlated with Cr_2O_3. The $Fe^{2+}/(Fe^{2+} + Mg)$ ratios of the analyzed grains display a limited range ($0.38 + 0.03/-0.04$), whereas Cr-numbers ($Cr/Cr + Al$) show greater variability ($0.79 + 0.08/-0.14$).

6. Discussion

The minimum Mg-numbers of the ultramafic tuff (0.80–0.88; calculated assuming all iron is ferrous) are significantly higher than those estimated for mantle-equilibrated primary liquids (~0.73; Farmer, 2003). The elevated Mg-numbers and scattering around the olivine-sorting line in Fig. 6A (see section 6.1) imply that the Stuhini Group ultramafic pyroclastic rocks have accumulated olivine, the most common and abundant phenocryst observed in these units.

6.1. Metamorphism, alteration, and element mobility

The ultramafic tuff of the Stuhini Group has been metamorphosed to greenschist facies as evidenced by the coexistence of serpentine, talc, chlorite, tremolite, and clinopyroxene. The serpentine-dominated assemblage implies metamorphism under low CO_2 activities ($X[CO_2]/X[H_2O] < 0.05$) and limits the maximum metamorphic temperatures to <550 °C (Bucher and Frey, 1994), assuming pressures <0.5 GPa (~15 km). The temperature of metamorphism of the ultramafic pyroclastic rocks must have reached >450 °C, as indicated by the presence of tremolite. The implied metamorphic temperatures suggest that the Mess Creek facies of the Stuhini Group were deposited prior to the emplacement of the Stikine plutonic suite (ca. 222 Ma; Logan et al., 2000; Milidragovic et al., 2016), which may have supplied the heat for metamorphism.

Olivine analyses from four samples yield a wide range of Fo contents (0.80–0.91). Given the relatively wide range of whole-rock MgO concentrations and the corresponding narrow range of Mg-numbers, the measured Fo contents suggest that relict olivine

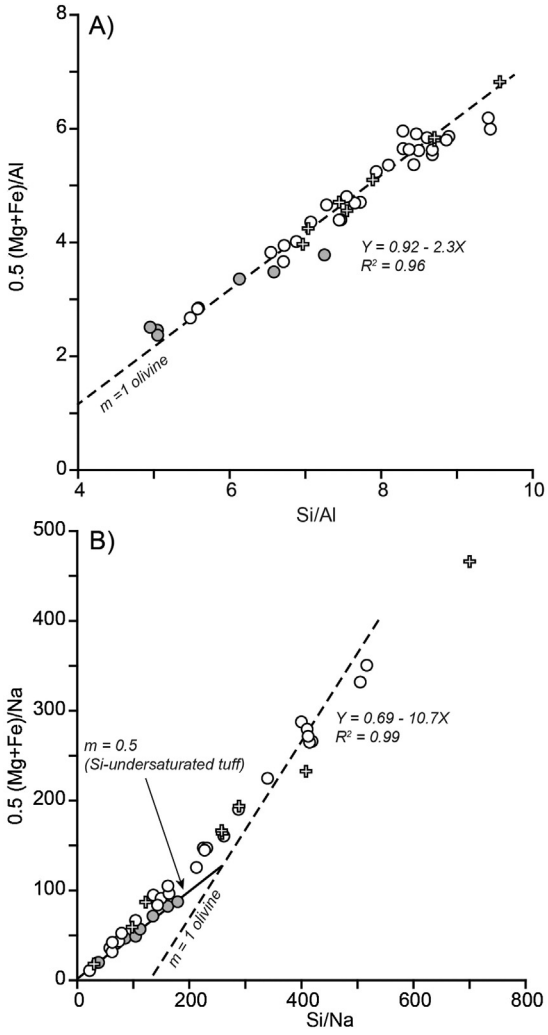

Fig. 6. Cation ratio plots using: Al (A) and Na (B) as denominator. Ideal olivine sorting line ($m = 1$; dashed line) is shown for reference, as is the result of linear regression through 35 samples reported in this study. The line, regressed through Ne-normative samples, is also shown in B).

has been significantly affected by low temperature element mobility. Significant element mobility in olivine is further supported by high Mn concentrations (1,500–17,000 ppm), which significantly exceed those of primitive olivine from common terrestrial magmas (<1600 ppm; e.g. Sobolev et al., 2007). Thus, the measured olivine compositions from Stuhini Group picrites, with the possible exception of the most Fo-rich analyses (Fo91; see discussion below), are not considered representative of magmatic compositions.

The contradictory Si-saturation indices of the coarse-grained tuff breccia and lapilli tuff and the fine-grained ash tuff in the very same section (Fig. 2) are of particular interest. The large amount of water involved, the positive volume change associated with serpentinization, and heating to >450 °C (see above) require an assessment of the mobility of major and trace elements during metamorphism of the ultramafic pyroclastic rocks of the Stuhini Group. Serpentinization of olivine in an open system increases the whole rock Si/Mg ratio (Kitayama and Francis, 2014), resulting in higher normative hypersthene content. Furthermore, loss of alkalies (Na_2O and K_2O) tends to drive the whole rock composition towards apparent Si-saturation, whereas addition of alkalies will drive the bulk rock towards Si-undersaturation. The poor observed correlation of elements that are typically immobile under sub-amphibolite facies metamorphic conditions (e.g. REE + Y, HFSE)

with SiO_2, K_2O, Na_2O and LILE suggests that the latter elements have experienced significant mobility. Similarly, the pronounced positive Sr anomaly, which characterizes all of the samples, cannot be attributed to accumulation of plagioclase. Instead, the anomalous enrichment of Sr in the pyroclastic rocks is attributed to alteration by sea-water or metamorphic fluids related to the local emplacement of the Stikine plutonic suite (Logan et al., 2000; Milidragovic et al., 2016).

Because the rocks show obvious petrographic and chemical evidence for olivine sorting, we used cation proportion ratio plots to investigate the mobility of individual elements (cf. Beswick, 1982). Samples of ultramafic tuff form a highly correlated arrays ($R^2 \geq 0.96$) with a slope of ~1 on plots of 0.5(Mg + Fe)/Al vs. Si/Al (Fig. 6A) and 0.5(Mg + Fe)/Ti vs. Si/Ti, indicating that the bulk of geochemical variation in MgO, FeO^{TOT}, SiO_2, TiO_2, and Al_2O_3 can be attributed to accumulation of olivine and that the effect of serpentinization on bulk rock Si/Mg ratio and these oxides is minor. In contrast, similar plots using Ca, Na or K as denominator yield slopes significantly less than one (Fig. 6B), implying highly non-conservative behavior. Importantly, nepheline-normative samples display the greatest deviation from the ideal olivine-controlled slope ($m = 1$) and define an array with an intercept of ~0. The Si-undersaturated, alkali-rich character of fine-grained ash tuff is, therefore, interpreted to reflect metasomatic gains in alkali metals during metamorphism. Consequently, the ultramafic tuffs of the Stuhini Group are considered to have a subalkaline magmatic affinity.

6.2. Thermometry and oxidation state

Chromite is the sole mineral phase that withstood the greenschist facies metamorphism and the pervasive serpentinization of the ultramafic tuff of the Stuhini Group (Electronic Appendix tables A4 and A5). The exchange of Fe^{2+} and Mg between chromite and olivine strongly depends on temperature and the occupancy of Cr, Al, and Fe^{3+} in the octahedral site of spinel. A number of calibrations have been proposed to quantify this dependence (Roeder et al., 1979; Fabriès, 1979; O'Neill and Wall, 1987; Ballhaus et al., 1991). In addition, O'Neill and Wall (1987) and Ballhaus et al. (1991) have formulated empirical equations that relate the chemistry of olivine-spinel pairs to fO_2 during crystallization. Temperatures and $\Delta \log fO_2$ values relative to the quartz–fayallite–magnetite (QFM) buffer, calculated at an assumed atmospheric pressure, are presented in Fig. 7. For these calculations, we assumed the composition of pre-metamorphic olivine (~Fo_{91}), deduced graphically using the intersection of the olivine control line defined by the tuff samples and the olivine stoichiometric line on the Mg vs. Fe diagram (Fig. 4). The assumed olivine Fo is identical to the highest Fo content of olivine measured using WDS. Although it is likely that chromite-olivine pairs equilibrated at $P > 1$ atm, the relative dependence of the calculated temperatures and $\Delta \log fO_2$ values on pressure is <2%/GPa and <30%/GPa, respectively. Two chromite analyses, which yielded $T > 1250\,^{\circ}C$, were obtained from a single chromite grain with a relatively low Cr/(Cr + Al + Fe^{3+}) ratio and a high MgO concentration (Fig. 7B). The geochemically anomalous grain derives from a distinct, possibly xenocrystic, population that appears unrelated to the main cognate population. Consequently the anomalously high temperatures recorded by the single chromite grain are not considered representative of the tuff's thermal history.

Application of the O'Neill and Wall (1987) and Ballhaus et al. (1991) olivine-spinel thermometers provides a range temperatures from 930–1180 °C (Fig. 7A). The highest temperatures were calculated from the most primitive chromite grains with highest (Cr/(Cr + Al + Fe^{3+}) ratios (≤0.82; Fig. 7C); consequently the minimum eruption temperature of the ultramafic pyroclastic rocks of the Stuhini Group was ~1200 °C. The calculated log fO_2 values relative to the FMQ buffer range from +1 in the most primitive chromites to +3 in the relatively evolved chromites (Fig. 7D). The minimum calculated value of log fO_2 = FMQ+1 is considered representative of the parental magma.

6.3. Parental magma composition

The high abundance of bubble-wall glass shards (Electronic Appendix B1), whose morphology is controlled by surface tension forces, in ash tuff beds is indicative of fragmentation by exsolution of magmatic volatiles, rather than by phreatomagmatic interaction of a hot magma with external water (Walker and Croasdale, 1972; Thompson Stiegler et al., 2011). Similarly, the ubiquity of "frothy" lapilli and the absence of accretionary lapilli are all indicative of explosive eruption driven primarily by exsolution of magmatic volatiles (Walker and Croasdale, 1972). Consequently, the Stuhini Group pyroclastic rocks are regarded as explosive products of an olivine-saturated ultramafic parental magma with a high magmatic H_2O content.

Olivine crystals within individual devitrified lapilli are typically euhedral and lack evidence of disequilibrium; they are, therefore, interpreted to be cognate products of magma crystallization rather than xenocryts entrained during its ascent through the lithosphere. The graphically-inferred composition of olivine constrains Mg/(Mg + Fe^{2+}) of the parental magma to ~0.76, assuming $K_D = 0.32$ (where $K_D = \frac{X^{ol}_{FeO} X^{liq}_{MgO}}{X^{ol}_{MgO} X^{liq}_{FeO}}$; e.g. Putirka et al., 2011). The volatile-free composition of the ultramafic parental magma can be calculated by incremental subtraction of olivine until the Mg/Fe ratio of the calculated liquid matches that of magma in equilibrium with Fo_{91}. In addition to the estimated olivine composition, the calculation also requires an estimate of the ferric/ferrous iron ratio of the parental magma. The optimal Fe^{3+}/Fe^{TOT} ratio was determined by simultaneously: 1) performing olivine-subtraction calculations at an assumed Fe^{3+}/Fe^{TOT} ratio (0.05–0.20) of the parental magma, and 2) using the equation of Kilinc et al. (1983), relating the Fe^{3+}/Fe^{TOT} ratio of the parental magma to its composition, fO_2, and temperature, constrained by olivine-spinel equilibria (Fig. 7). Optimal agreement between the assumed Fe^{3+}/Fe^{TOT} ratio and that calculated using the parametrization of Kilinc et al. (1983) was found at $Fe^{3+}/Fe^{TOT} = 0.12$. The corresponding Fe^{3+}/Fe^{TOT} ratio of the parental magma calculated using the parametrization of Kilinc et al. (1983) is $0.13 + 0.05/-0.03$.

Our calculations suggest that the ultramafic pyroclastic rocks of the Stuhini Group formed by ~20–65% accumulation of olivine into a picritic parental magma with ~16 ± 1 wt.% MgO (Table 2; Fig. 4; Electronic Appendix Table A6; see also Milidragovic et al., 2016). The calculated parental concentrations of MgO, FeO^{TOT} (10 ± 1 wt.%), Al_2O_3 (10 ± 1 wt.%), and TiO_2 (0.6 ± 0.1 wt.%) show a high degree of consistency across the suite. In contrast, concentrations of SiO_2 ($50 + 4/-5$ wt.%), CaO ($11 + 5/-4$ wt.%), and especially K_2O ($0.3 + 1.2/-0.2$ wt.%) and Na_2O ($0.3 + 4/-0.2$ wt.%), in the parental magma display a relatively large range and are consistent with the greater mobility of these elements during metamorphism and alteration. The concentration of Ni in the parental magma (~430 ppm) was estimated by linearly extrapolating the Ni–MgO array (Fig. 3C) to the MgO concentration of parental magma (16 wt.%).

The trace element of content of the picritic magma parental to the Stuhini Group tuff was calculated by subtracting olivine from each sample using the calculated accumulation fractions and distribution coefficients for olivine, estimated using the parametrization of Bédard (2005) for liquids with MgO = 16 wt.%. The calcu-

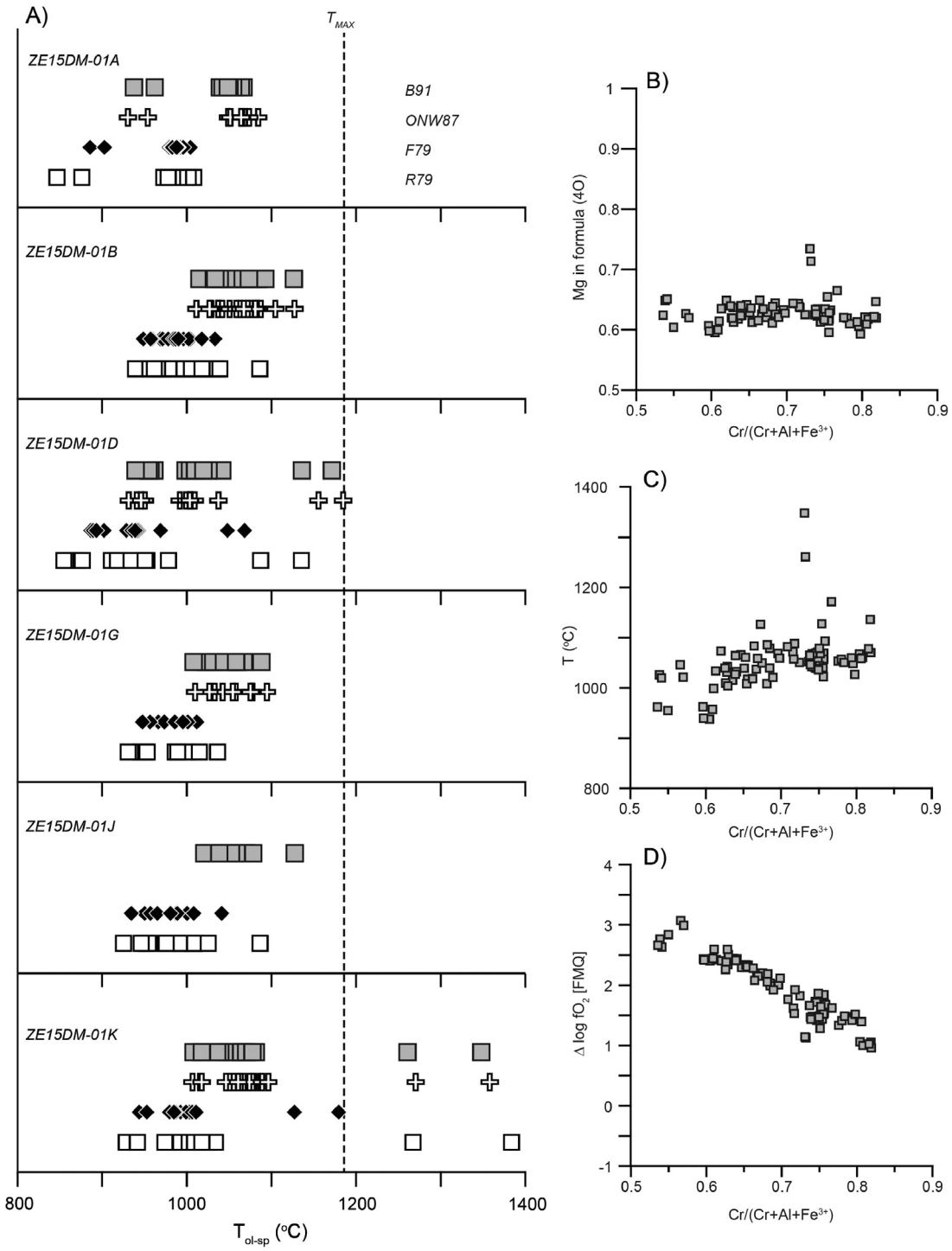

Fig. 7. Olivine-spinel equilibration temperatures (°C) from individual chromite analyses grouped by sample and calculated using the calibrations of Roeder et al. (1979; R79), Fabriès (1979; F79), O'Neill and Wall (1987; ONW87), and Ballhaus et al. (1991; B91). See top panel for symbol explanation. B) Mg cations in formula unit (based on 4O) vs. $Cr/(Cr + Al + Fe^{3+})$. C) Olivine-spinel equilibration temperature (°C) calculated using the thermometer of Ballhaus et al. (1991) vs. $Cr/(Cr + Al + Fe^{3+})$. D) $\Delta \log fO_2$ [FMQ] calculated using the oxybarometer of Ballhaus et al. (1991) vs. $Cr/(Cr + Al + Fe^{3+})$.

lated liquid has higher overall abundance of trace elements than the analyzed tuff samples (Fig. 5), but retains the overall calc-alkaline arc pattern of LILE and LREE enrichment and HFSE depletion (Ulmer, 2001 and references therein) that characterizes individual tuff samples. Notably, the calculated abundance of MREE and HREE in the parental picrite is significantly less than in MORB ($Yb_{MORB} = 0.3–0.4$). Furthermore, the calculated parental liquid has a low Nb/Zr ratio ($0.03 + 0.05/-0.01$) similar to that of N-MORB (0.03; Sun and McDonough, 1989).

6.4. Constraints on the mantle wedge processes and the geodynamic model for generation of picritic melts in arc settings

Logan and Mihalynuk (2014) suggested that the wide-spread occurrence of Middle to Late Triassic picritic magmatism in the Canadian Cordillera (Russell and Snyder, 1997; Logan et al., 2000) is indicative of elevated temperatures in the underlying mantle wedge. Thermal perturbations, proposed by Logan and Mihalynuk (2014), were attributed to tearing of the subducting Panthalassan

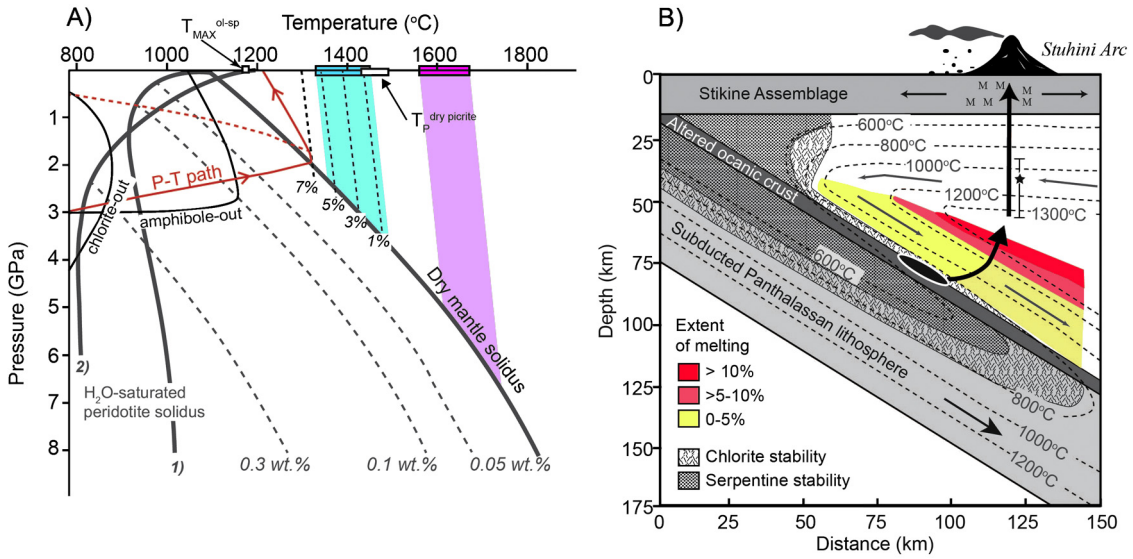

Fig. 8. A) P (GPa) vs. T (°C) diagram showing the dry mantle solidus (Katz et al., 2003), and water saturated solidi from 1) Katz et al. (2003) and Grove et al. (2009). Chlorite (Grove et al., 2009) and pargasite (Green et al., 2014) stability fields (thin solid black lines), and peridotite solidii (grey dashed lines) for bulk water contents of 0.05, 0.1, and 0.3 wt.% are also shown. The white rectangle along abscissa ($T_P^{\text{dry picrite}}$) is the potential temperature of picrite parental magmas calculated assuming a dry composition and using equations of Putirka (2008) and Putirka (2016). The black dashed lines show the reduction in potential temperature at the given H_2O concentration in the magma. The white square along abscissa ($T_{MAX}^{\text{ol-sp}}$) is the maximum calculated olivine-spinel equilibration temperature. The blue and pink fields correspond to the potential temperatures of MORB (ambient mantle), and Hawaiian mantle sources. The solid red path illustrates a hypothetical path that a melt generated at $P \geq 3$ GPa may take through the mantle wedge and overlying lithosphere. The dashed red line is a path, which remains in thermal equilibrium with its surroundings as it crosses the normal geothermal gradient of the uppermost arc mantle and lithosphere. B) A schematic section through a subduction zone (modified from Grove et al., 2009) showing the salient features of our model. Dehydration of subducting slab at 2.5–3 GPa (black elipse; van Keken et al., 2011) leads to overstepping of the water-saturated solidus and hydrous flux melting up the geothermal gradient. Because of the coupling of the subducting slab and the overlying mantle (thin grey arrows), the melting column (thick black arrow) is not necessarily vertical. In the hot nose of the wedge, where $T > 1300$ °C, melting may exceed 10% ($F > 0.1$) and water-rich picritic melts are generated. The estimated pressure of equilibration ($1.2 + 0.5/-03$ GPa; star with error bars) reflects the depth at which melts last equilibrated. The ascent across the upper part of mantle wedge and through Stikinia's lithosphere is adiabatic and driven by high buoyancy of the hydrous picritic magma (illustrated by the vertical ascent path) and lithospheric extension (horizontal black arrows). Hot water-rich melts may be an efficient transport agent of base and precious metals from the mantle into the crust of Stikinia (schematically shown by "M").

slab and ingress of sub-slab asthenosphere into the mantle wedge. Their proposed model was largely influenced by the widespread belief that picritic magmas require anomalously high melting temperatures (e.g. Nye and Reid, 1986; Wilson, 2003), a view biased by the more abundant and more extensively studied ultramafic magmas in intraoceanic settings (e.g. Herzberg et al., 2010; Putirka et al., 2011). The relatively low eruption temperatures of the Stuhini Group picrites (~1200 °C) are, however, >200 °C lower than the expected temperatures of comparably-magnesian anhydrous liquids (Ulmer, 2001). Furthermore, the low Nb/Zr ratios of the Stuhini Group picrites suggest derivation from a depleted mantle source and do not support significant contribution of sub-slab asthenosphere, normally manifested by high Nb/Zr ratios similar to those of E-MORB or ocean intraplate basalts (OIB; e.g. Mullen and Weis, 2015). The high Mg-number and MgO concentration of the calculated parental magmas, and the high inferred Fo content of the accumulated olivine phenocrysts, suggest that the ultramafic pyroclastic rocks of the Stuhini Group formed from near-primary, mantle-equilibrated magmas. Consequently, the calculated magma compositions and the inferred compositions of olivine phenocrysts provide unique insight into the thermal and compositional character of the picrite mantle source.

Pressure-dependent activity of SiO_2 in peridotite-equilibrated melts is the basis of empirical relationships used to estimate the depth of equilibration between Stuhini Group picrites and their source mantle. The equilibration pressure for the full suite of samples, calculated using the barometer of Putirka (2008), is $1.3 + 1.1/-0.4$ GPa. The error on the calculated pressure of equilibration is significantly reduced when only Si-saturated samples, plotting along the olivine-controlled sorting line (Fig. 6A), are considered ($P = 1.2 + 0.5/-0.3$ GPa; Table 2). The modified relationship developed by Lee et al. (2009), which incorporates a relatively negligible dependence on H_2O, provides a similar estimate of equilibration pressure for the Stuhini Group picrites ($1.2 + 0.5/-0.4$ GPa).

Putirka (2016) developed an empirical equation relating melt composition to the degree of melting of the terrestrial mantle. Melt fractions ($F = 0.13 + 0.03/-0.05$), estimated using the Si-saturated parental magmas only, are slightly higher than estimates for primitive MORB (~0.10; Lee et al., 2009; Putirka et al., 2011) and comparable to melt fractions ($F = 0.14$–0.17) invoked in genesis of similarly magnesian liquids from model depleted peridotite (DMM1; Wasylenki et al., 2003). The estimated degree of melting, calculated using anhydrous olivine-liquid temperature (see below), and the solidus and liquidus curves for an assumed anhydrous mantle composition (Putirka, 2016) is significantly higher ($0.23 + 0.06/-0.03$). This second approximation probably overestimates the degree of melting given the likely volatile-rich composition of the Stuhini Group picrites, indicated by the abundance of scoriaceous fragments, the well-known depression of peridotite solidi with increased H_2O content (Green, 1973; Katz et al., 2003; Grove et al., 2006), and the tendency of H_2O to decrease melt productivity (in terms of melt fraction/°C) at $F \leq 0.25$ (Gaetani and Grove, 1998; Katz et al., 2003; Kelley et al., 2010). Nevertheless, both estimates are significantly lower than the estimated 50% melting, suggested by Logan and Mihalynuk (2014). In the light of our estimate of moderate degrees of melting ($F = 0.10$–0.15), the low absolute abundance of immobile trace elements in the parental picritic liquid ($Yb_{MORB} = 0.3$–0.4) indicates that the mantle source of the Stuhini Group picrite was depleted relative to the source of MORB.

The positive dependence of the MgO content of a primitive magma and the Fo content of its olivine on temperature is

Table 2
Estimated composition of the Stuhini Group picrite parental magma.

Major elements (wt.%)		
SiO_2	49.2	+3.6/−4.6
TiO_2	0.57	+0.10/−0.05
Al_2O_3	9.9	+1.4/−1.2
Cr_2O_3	0.76	+0.24/−0.39
Fe_2O_3	0.88	+0.08/−0.07
FeO	9.9	+0.8/−0.7
MnO	0.31	+0.08/−0.10
MgO	15.8	+1.4/−1.2
CaO	11.3	+5.0/−4.1
Na_2O	0.27	+4.06/−0.22
K_2O	0.26	+1.19/−0.17
P_2O_5	0.16	+0.06/−0.04
Total	100.0	
Intrinsic properties		
$T_{MAX\ ol\text{-}sp}$ (°C)[a]	1135	
$T_{MAX\ ol\text{-}sp}$ (°C)[b]	1068	
$T_{MAX\ ol\text{-}sp}$ (°C)[c]	1185	
$T_{MAX\ ol\text{-}sp}$ (°C)[d]	1171	
$\Delta \log f O_2$(FMQ)[d]	+1	
Fe^{3+}/Fe^{TOT}[e]	0.13	+0.05/−0.03
P (GPa)[f]	1.2	+0.5/−0.3
P (GPa)[g]	1.2	+0.5/−0.4
F[h]	0.13	+0.03/−0.05
T_{liq} (°C)[i]-dry (1 atm)	1411	+38/−30
T_{liq} (°C)[j]-dry (1 atm)	1408	+44/−26
T_{liq} (°C)[k]-dry	1445	+41/−39
$T_{ol\text{-}liq}$ (°C)[l]-dry (P^f)	1427	+58/−28
$T_{ol\text{-}liq}$ (°C)[m]-dry (P^f)	1411	+49/−30
T_P (°C)[n]-dry	1461	+33/−32
T_P (°C)[o]-1% H_2O	1436	+32/−31
T_P (°C)[o]-3% H_2O	1387	+30/−30
T_P (°C)[o]-5% H_2O	1341	+29/−29
T_P (°C)[o]-7% H_2O	1298	+28/−27

Trace elements (ppm)		
Cs	1.0	+1.9/−0.3
Rb	11	+57/−8
Ba	158	+1105/−139
Th	0.36	+0.31/−0.08
U	0.28	+0.17/−0.04
Nb	0.8	+1.1/−0.4
Ta	0.09	+0.22/−0.06
Sr	270	+360/−140
Zr	28	+10/−5
Hf	0.7	+0.3/−0.3
Y	10.7	+1.8/−1.2
Sc	32	+3/−3
Co	50	+4/−13
Zn	65	+43/−11
Cr	2270	+450/−500
Ni	290	+50/−25
La	3.5	+3.2/−0.7
Ce	7.2	+6.9/−0.7
Pr	1.0	+0.7/−0.2
Nd	5.0	+2.1/−0.8
Sm	1.5	+0.5/−0.3
Eu	0.53	+0.18/−0.11
Gd	1.8	+0.4/−0.3
Tb	0.31	+0.07/−0.04
Dy	1.9	+0.07/−0.04
Ho	0.37	+0.09/−0.07
Er	1.1	+0.2/−0.2
Tm	0.15	+0.03/−0.03
Yb	1.0	+0.2/−0.1
Lu	0.15	+0.03/−0.02

Reported values are median abundances and the associated 95th percentile confidence intervals ($n = 43$).
[a] Olivine-spinel thermometer of Roeder et al. (1979).
[b] Olivine-spinel thermometer of Fabriès (1979).
[c] Olivine-spinel thermometer of O'Neill and Wall (1987).
[d] Olivine-spinel thermometer and oxybarometer of Ballhaus et al. (1991).
[e] Fe^{3+}/Fe^{TOT} after Kilinc et al. (1983).
[f] Silica-activity barometer of Putirka (2008; eq. 42) calculated using T_{liq} of Putirka (2008).
[g] Silica-activity barometer of Lee et al. (2009; eq. 2) calculated using T_{liq} of Lee et al. (2009).
[h] Melt fraction (Putirka, 2016; eq. 14b).
[i] Liquid thermometer of Helz and Thornber (1987), modified by Putirka (2008).
[j] Liquid thermometer of Putirka (2008; eq. 14).
[k] Liquid thermometer of Lee et al. (2009; eq. 3).
[l] Olivine-liquid thermometer of Beattie (1993).
[m] Olivine-liquid thermometer of Putirka (2008; eq. 22).
[n] T_P (°C) calculated from eq. 12c of Putirka (2016), assuming $T_{ol\text{-}liq}$ of Putirka (2008) for primary magma with 0% H_2O.
[o] T_P calculated assuming primary magma with $1 \leq H_2O \leq 7$ wt.%.

well known (e.g. Hanson and Langmuir, 1978) and is the basis for liquid-only and olivine-liquid thermometers (see review by Putirka, 2008). Calculations on nominally anhydrous primary picrite compositions provide an estimate of the maximum equilibrium temperature of the Stuhini Group picrites and the potential temperature of their mantle source (T_P; Table 2). Median anhydrous equilibration temperatures calculated from Si-saturated parental liquid compositions using both liquid compositions (Hels and Thornber, 1987; Putirka, 2008; Lee et al., 2009) and olivine-liquid pairs (Beattie, 1993; Putirka, 2008) range between 1410 and 1450 °C, and translate into mantle T_P of ~1450–1500 °C, using the model of Putirka (2016). Potential temperatures, calculated assuming nominally anhydrous picrite compositions, are intermediate between the T_P of ambient mantle (1330–1450 °C) and the T_P of Phanerozoic intraplate basalts (1450–1650 °C), which are widely attributed to anomalous thermal plumes (Putirka, 2008; Herzberg et al., 2010; Putirka, 2016). Taken at face value, the calculated T_P values of the Stuhini Group picrites require a mantle source that is hotter than the ambient Phanerozoic mantle.

Presence of water in the mantle source and the resulting picritic melt dramatically reduces the temperature of melting (e.g. Green, 1973; Katz et al., 2003; Grove et al., 2006). Melt inclusion data suggests that primary mafic arc lavas contain a range of H_2O concentrations of 2–6 wt.%, with an apparent global average of ~3.5 wt.% (e.g. Plank et al., 2013). Primary H_2O concentrations >6 wt.%, however, have been measured from individual volcanoes (Vigouroux et al., 2008). Assuming H_2O concentrations of 1 to 7 wt.% for hydrous primary magmas parental to the Stuhini Group picrites, would lower their estimated mantle T_P between ~1410 and 1300 °C (±30 °C). Notably, mantle T_P, calculated assuming relatively high H_2O content (5–7 wt.%) of the Stuhini Group picrites overlap, or are slightly less than, estimates of the ambient MORB-source mantle (Fig. 8). Furthermore, these temperatures are more consistent with the maximum temperatures obtained from olivine-spinel equilibria (≥1180 °C; Fig. 7), which overlap experimental crystallization temperatures of hydrous Mg-rich arc magmas (Ulmer, 2001; Nandedkar et al., 2014). The mantle source for the hypothetical hydrous primary melts (H_2O = 5–7 wt.%), cal-

culated assuming batch mantle melting and a mantle-liquid H_2O partition coefficient of 0.008 (Hirschmann et al., 2009), would contain 0.7–0.9 wt.% H_2O. A comparable concentration of H_2O has been invoked by Kelley et al. (2010) and Plank et al. (2013) for the mantle source of the Mariana arc lavas (0.6–1.0 wt.%).

Excess water, required to depress the mantle solidus and initiate melting at lower T may have originated from breakdown of chlorite (Grove et al., 2006, 2009), pargasite (Green et al., 2014), or a more complex metamorphic assemblage (van Keken et al., 2011) during the progressive metamorphism and dehydration of the subducting Panthalassan plate. Combined thermal and petrological modeling by van Keken et al. (2011) suggests that dehydration in intermediate-temperature subduction zones, such as the southern Marianas subduction zone, releases water from the upper crust in the interval 2.5–3 GPa (80–100 km). In contrast, they infer slab dehydration in hot subduction zones to be nearly complete by the 80 km depth, whereas in cold subduction zones upper crustal and mantle dehydration is less efficient, proceeding to significantly greater depths. At pressures of 2–4 GPa, the breakdown of hydrous minerals in the subducting slab occurs at temperatures exceeding the H_2O-saturated peridotite solidus (Fig. 8), resulting in immediate melt production. As buoyant hydrous melts rise across the inverse geothermal gradient of the lower portion of the mantle wedge, the degree of melting increases, reaching maximum in the hot nose of the mantle wedge (Fig. 8; Grove et al., 2009). Numerical models of mantle wedge thermal structure indicate that the nose of the wedge may attain temperatures in excess of 1300 °C at relatively low pressures ($\leq$2 GPa; Kelemen et al., 2003), provided that mantle viscosity is temperature-dependent and the angle of subduction is relatively steep ($\geq$30°; Grove et al., 2009: Fig. 8). Relatively steep subduction would also restrict the interval of dehydration in the downgoing slab, consequently limiting the width of the overlying arc (Grove et al., 2009) and, perhaps importantly, confining flux melting to a relatively narrow, anomalously hydrous column. This model differs markedly from the model of Logan and Mihalynuk (2014) in that it does not require tearing of the subducting slab or other special tectonic scenarios, such as ridge or transform fault subduction (Rohrbach et al., 2005), back-arc spreading (Yamamoto, 1988), or crustal delamination in which anomalously high geothermal gradients are induced in the mantle wedge through inflow of asthenosphere. Instead, our model relies on efficient dehydration of the subducting Panthalassan plate and ascent of water-rich melts into the moderately hot mantle wedge nose in a setting similar to the modern-day south Marianas arc (van Keken et al., 2011).

Despite this relatively simple model, the near-primary character of the Stuhini Group picrites makes them part of a rare population of primitive arc magmas. Arc magmas must traverse the uppermost arc mantle and lithosphere, which are characterized by a normal geothermal gradient (Fig. 8). The primitive chemistry of the Stuhini Group picrites requires a near-adiabatic path in which conductive exchange with the upper mantle wedge and lower crust is minimal, allowing the ascending magma to preserve its primary composition. In contrast, slow rise and attainment of thermal equilibrium with the ambient rocks through conductive cooling would result in fractional crystallization of olivine and evolution of melt composition. Adiabatic ascent through the upper mantle wedge and the overlying arc crust is favored by the relatively high inferred water content of the primary picritic magma, and its resulting high relative buoyancy and low viscosity (Electronic Appendix B3).

The Middle- to Upper Triassic Stuhini Group contains abundant marine fossils, including radiolarians, conodonts, corals, bivalves, and brachiopods (Mihalynuk et al., 1999; Logan et al., 2000), indicating a low-lying, predominantly mafic and relatively dense arc. The prolonged history of submarine volcanism suggests that the Stuhini arc was likely undergoing moderate extension, consequently never emerging above the sea level for significant periods of time (at least 15 m.y.). A predominantly extensional state of the Stuhini arc would further favor rapid ascent of rapidly-devolatilizing, explosive picrite magma through the thin Stikine arc crust, minimizing water loss and fractional crystallization of olivine above vapour-saturation pressures (0.3–0.5 GPa; Plank et al., 2013). Consequently, the explosive mode of emplacement of the Stuhini Group picrites may be the norm rather than anomaly for emplacement of arc picrites.

The water-rich and oxidized nature of the Middle- to Late Triassic picrites may also be key to mobilization and transport of metals from the asthenospheric mantle wedge into the sub-arc lithospheric mantle and lower crust of the Stikine terrane, and the Late Triassic Cu–Mo(–Au) porphyry mineralization. Their relatively elevated fO_2 ($\log fO_2 \geq \mathrm{FMQ}+1$) would have stabilized soluble sulfate and suppressed sulfide saturation, leading to partitioning of mantle copper, molybdenum and other chalcophile and weakly siderophile elements into the silicate melt (Richards, 2011, and references therein). Similar high-MgO, moderately oxidised basaltic magmas have been invoked as the primary vectors for movement of mantle metals into the lower crust, where they pond within the MASH (melting, assimilation, storage, homogenization) zone and undergo calc-alkaline fractional crystallization and assimilation of crustal rocks to produce the high-H_2O intermediate magmas that are principally associated with formation of porphyry mineral deposits. As demonstrated above, Stuhini picritic magmas apparently did not achieve neutral buoyancy during their ascent through the crust and so would not have been subject to MASH zone modification processes. However, their appearance in the lowermost portions of the Stuhini volcanic succession suggests that their extreme buoyancy and presumed low viscosity may have played a key role in ground preparation and conduit development that facilitated the ascent of later magmas.

7. Concluding remarks

Ultramafic tuff breccia, lapilli tuff, and ash tuff were deposited on the Stikine terrane of the North American Cordillera as part of the Middle- to Upper Triassic Stuhini Group. Their high MgO content and low abundances of Al_2O_3, TiO_2, and immobile incompatible trace elements reflect 20–65 % accumulation of olivine into a subalkaline picritic parental melt with $\geq$16 wt.% MgO (LOI-free). Thermobarometric calculations indicate that the parental magmas were moderately oxidized ($\log fO_2 \sim \mathrm{FMQ}+1$) and erupted at temperatures $\geq$1180 °C. Olivine-liquid thermometry, which is highly sensitive to the concentration of H_2O dissolved in the melt, suggests that anomalously high temperatures did not occur in the mantle source of the picrites, but that it likely contained above-average H_2O concentrations (5–7 wt.%). The estimated degree of melting that generated the Stuhini Group picrites (10–15%) is only slightly above that inferred for MORB ($\sim$10%).

Our proposed model of moderate degree melting under ordinary mantle wedge thermal conditions contrasts with the existing model for genesis of primitive, picritic magmas in arc settings. Our model requires, however, a relatively efficient release of slab fluids in the limited interval between $\sim$2.5–3.0 GPa in order to generate water-rich, moderate-degree melts in the hot nose of the mantle wedge. This model also implies a near-adiabatic ascent of hydrous picritic melts through the mantle wedge and into the crust. Physicochemical conditions during the genesis of picritic melts within the mantle wedge beneath the Stuhini arc do not appear to have differed significantly from conditions inferred from previous studies of 'normal' convergent margin magmatism. Indeed, many of the parameters constrained by this work (e.g. fO_2, T_P, F) are within or only slightly above their range of variability

identified from other arc systems globally (Richards, 2011, and references therein). Hence, rather than reflecting unusual degrees of melt generation or exceptional heat flux, hydrous picritic melting may be common within arc magmatic systems, but may be, subsequently, diluted out by later basaltic melts or re-equilibration during ascent. Appearance of picritic volcaniclastic sequences within the Stuhini volcanic pile may reflect exceptional preservation of near-primary magmas by ascent through thin, faulted and attenuated island arc crust, rather than unusual melt generation.

Acknowledgements

This project is funded by the Government of Canada's Geo-Mapping for Energy and Minerals program (GSC contribution 29874), with logistical support from Teck Resources. G. Jutras, L. Bailey, and K. Heppe of Teck facilitated our fieldwork out of the Schaft Creek exploration camp. S. Carroll provided excellent assistance in the field. E. Czech, L. Kato, and M. Raudsepp provided valuable assistance with the microanalytical work at UBC. The manuscript benefited from comments by M.J. Bickle, K. Putirka, and an anonymous reviewer.

Appendix A. Supplementary material

Supplementary material related to this article can be found online at http://dx.doi.org/10.1016/j.epsl.2016.08.034.

References

Ballhaus, C., Berry, R.G., Green, D.H., 1991. High pressure experimental calibration of the olivine-orthopyroxene-spinel oxygen geobarometer: implications for the oxidation state of the upper mantle. Contrib. Mineral. Petrol. 107, 27–40.

Barresi, T., Nelson, J.L., Dostal, J., Friedman, R., 2015. Evolution of the Hazelton arc near Terrace, British Columbia: stratigraphic, geochronological, and geochemical constraints on a Late Triassic–Early Jurassic arc and Cu–Au belt. Can. J. Earth Sci. 52, 466–494.

Bédard, J.H., 2005. Partitioning coefficients between olivine and silicate melts. Lithos 83, 394–419.

Beattie, P., 1993. Olivine-melt and orthopyroxene-melt equilibria. Contrib. Mineral. Petrol. 115, 103–111.

Beswick, A.E., 1982. Some geochemical aspects of alteration and genetic relations of komatiites suites. In: Arndt, N.T., Nisbet, E.G. (Eds.), Komatiites. Allen and Unwin, London, pp. 283–308.

Bucher, K., Frey, M., 1994. Petrogenesis of Metamorphic Rocks, 6th ed. Springer-Verlag, Berlin, Heidelberg. 318 pp.

Cooke, D.R., Hollings, P., Walshe, J.L., 2005. Giant porphyry deposits: characteristics, distribution, and tectonic controls. Econ. Geol. 100, 801–818.

Eggins, S.M., 1993. Origin and differentiation of picritic arc magmas, Ambae (Aoba), Vanuatu. Contrib. Mineral. Petrol. 114, 79–100.

Fabriès, J., 1979. Spinel-olivine geothermometry in peridotites from ultramafic complexes. Contrib. Mineral. Petrol. 69, 329–336.

Farmer, G.L., 2003. Continental basaltic rocks. In: Rudnick, R.L. (Ed.), Treatise on Geochemistry, vol. 3. Elsevier, Amsterdam, pp. 85–121.

Gaetani, G.A., Grove, T.L., 1998. The influence of water on melting of peridotite. Contrib. Mineral. Petrol. 131, 323–346.

Green, D.H., 1973. Experimental melting studies on a model upper mantle composition at high pressure under water-saturated and water-undersaturated condition. Earth Planet. Sci. Lett. 19, 37–53.

Green, D.H., Hibberson, W.O., Rosenthal, A., Kovács, I., Yaxley, G.M., Falloon, T.J., Brink, F., 2014. Experimental study of the influence of water on melting and phase assemblages in the upper mantle. J. Petrol. 55, 2067–2096.

Grove, T.L., Till, C.B., Krawczynski, M.J., 2006. The influence of H_2O on mantle wedge melting. Earth Planet. Sci. Lett. 249, 74–89.

Grove, T.L., Till, C.B., Chatterjee, N., Medard, E., 2009. Kinematic variables and water transport control the formation and location of arc volcanoes. Nature 459, 694–697.

Hanson, G.N., Langmuir, C.H., 1978. Modelling of major elements in mantle-melt systems using trace element approaches. Geochim. Cosmochim. Acta 42, 725–741.

Hart, C.J.R., 1997. A transect across Northern Stikinia: geology of the Northern Whitehorse map area, Southern Yukon Territory (105D/13-16). In: Exploration and Geological Services Division, Yukon, Indian and Northern Affairs Canada, Bulletin 8. 113 pp.

Helz, R.T., Thornber, C.R., 1987. Geothermometry of Kilauea Iki lava lake, Hawaii. Bull. Volcanol. 49, 651–668.

Herzberg, C., Condie, K., Korenaga, J., 2010. Thermal history of the Earth and its petrological expression. Earth Planet. Sci. Lett. 292, 79–88.

Hirschmann, M.M., Tenner, T., Aubaud, C., Withers, A.C., 2009. Dehydration melting of nominally anhydrous mantle: the primacy of partitioning. Phys. Earth Planet. Inter. 176, 54–68.

Kamenetsky, V.S., Sobolev, A.V., Joron, J.L., Semet, P., 1995. Petrology and geochemistry of Cretaceous ultramafic volcanics from Eastern Kamchatka. J. Petrol. 36, 637–662.

Katz, R.F., Spiegelman, M., Langmuir, C.H., 2003. A new parametrization of hydrous mantle melting. Geochem. Geophys. Geosyst. 4. http://dx.doi.org/10.1029/2002GC000433.

Kelemen, P.B., Rilling, J.L., Parmentier, E.M., Mehl, L., Hacker, B.R., 2003. Thermal structure due to solid-state flow in the mantle wedge beneath arcs. In: Eiler, J.M. (Ed.), Inside the Subduction Factory. In: Geophys. Monogr., vol. 138. Am. Geophys. U., pp. 293–311.

Kelley, K.A., Plank, T., Newman, S., Stolper, E.M., Grove, T.L., Parman, S., Hauri, E.H., 2010. Mantle melting as a function of water beneath the Mariana arc. J. Petrol. 51, 1711–1738.

Kilinc, A., Carmichael, I.S.E., Rivers, M.L., Sack, R.O., 1983. The ferric-ferrous ratio of natural silicate liquids equilibrated in air. Contrib. Mineral. Petrol. 83, 136–140.

Kitayama, Y.C., Francis, D., 2014. Iron-rich alkaline magmatism in the Archean Wawa greenstone belts (Ontario, Canada). Precambrian Res. 252, 53–70.

Lee, C.-T.A., Luffi, P., Plank, T., Dalton, H., Leeman, W.P., 2009. Constraints on the depths and temperatures of basaltic magma generation on Earth and other terrestrial planets using new thermobarometers for mafic magmas. Earth Planet. Sci. Lett. 279, 20–33.

Logan, J.M., Mihalynuk, M.G., 2014. Tectonic controls on early Mesozoic paired alkaline porphyry deposit belts (Cu–Au ± Ag–Pt–Pd–Mo) within the Canadian Cordillera. Econ. Geol. 109, 827–858.

Logan, J.M., Drobe, J.R., McClelland, W.C., 2000. Geology of the Forrest Kerr-Mess Creek Area, Northwestern British Columbia (NTS 104B/10, 15 & 104/G2 & 7W). In: British Columbia Geological Survey Bulletin, vol. 104. British Columbia Ministry of Energy, Mines and Petroleum Resources. 164 pp.

Mihalynuk, M.G., Mountjoy, K.J., Smith, M.T., Currie, L.D., Gabites, J.E., Tipper, H.W., Orchard, M.J., Poulton, T.P., Cordey, F., 1999. Geology and mineral resources of the Tagish Lake area (NTS 104M/ 8, 9, 10E, 15 and 104N/12W), northwestern British Columbia. In: British Columbia Geological Survey Bulletin 8. British Columbia Ministry of Energy and Mines. 217 pp.

Milidragovic, D., Joyce, N.L., Zagorevski, A., Chapman, J.B., 2016. Petrology of explosive Middle–Upper Triassic ultramafic rocks in the Mess Creek area, northern Stikine terrane. In: Geological Fieldwork 2015. In: British Columbia Geological Survey Paper, vol. 2016-1. British Columbia Ministry of Energy and Mines, pp. 95–111.

Mullen, E.K., Weis, D., 2015. Evidence for trench-parallel mantle flow in the northern Cascade Arc from basalt geochemistry. Earth Planet. Sci. Lett. 414, 100–107.

Nandedkar, R.H., Ulmer, P., Müntener, O., 2014. Fractional crystallization of primitive, hydrous arc magmas: an experimental study at 0.7 GPa. Contrib. Mineral. Petrol. 167, 1015–1042.

Nelson, J., Colpron, M., Israel, S., 2013. The Cordillera of British Columbia, Yukon and Alaska: tectonics and metallogeny. In: Colpron, M., Bissig, T., Rusk, B., Thompson, J.F.H. (Eds.), Tectonics, Metallogeny, and Discovery – the North American Cordillera and Similar Accretionary Settings. In: Soc. Econ. Geol., Spec. Pub., vol. 17, pp. 53–109.

Nye, C.J., Reid, M., 1986. Geochemistry of primary and least fractionated lavas from Okmok volcano, central Aleutians: implications for arc magma genesis. J. Geophys. Res. 91, 10271–10287.

O'Neill, H.St.C., Wall, V.J., 1987. The olivine-orthopyroxene-spinel oxygen geobarometer, the nickel precipitation curve, and the oxygen fugacity of the Earth's upper mantle. J. Petrol. 28, 1169–1191.

Palme, H., O'Neill, H.St.C., 2003. Cosmochemical estimates of mantle composition. In: Holland, H.D., Turekian, K.K., Davis, A.M. (Eds.), Treatise on Geochemistry, vol. 2. Elsevier, Amsterdam, The Netherlands, pp. 1–38.

Plank, T., Kelley, K.A., Zimmer, M., Hauri, E.H., Wallace, P.J., 2013. Why do mafic arc magmas contain ~4 wt.% water on average? Earth Planet. Sci. Lett. 364, 168–179.

Putirka, K.D., 2008. Thermometers and barometers for volcanic systems. Rev. Mineral. Geochem. 69, 61–120.

Putirka, K.D., 2016. Rates and styles of planetary cooling on Earth, Moon, Mars, and Vesta, using new models for oxygen fugacity, ferric-ferrous ratios, olivine-liquid Fe–Mg exchange, and mantle potential temperature. Am. Mineral. 101, 819–840.

Putirka, K.D., Ryerson, F.J., Perfit, M., Ridley, W.I., 2011. Mineralogy and composition of the oceanic mantle. J. Petrol. 52, 279–313.

Richards, J.P., 2011. Magmatic to hydrothermal metal fluxes in convergent and collided margins. Ore Geol. Rev. 40, 1–26.

Roeder, P.L., Campbell, I.H., Jamieson, H.E., 1979. A re-evaluation of the olivine-spinel geothermometer. Contrib. Mineral. Petrol. 68, 325–334.

Rohrbach, A., Schuth, S., Ballhaus, C., Münker, C., Matveev, S., Qopoto, C., 2005. Petrological constraints on the origin of arc picrites, New Georgia Group, Solomon Islands. Contrib. Mineral. Petrol. 149, 685–698.

Russell, J.K., Snyder, L.D., 1997. Petrology of picritic basalts from Kamloops, British Columbia: primary liquids from a Triassic–Jurassic arc. Can. Mineral. 35, 521–541.

Sobolev, A.V., Hofmann, A.W., Kuzmin, D.V., Yaxley, G.M., Arndt, N.T., Chung, S.-L., Danyushevsky, L.V., Elliott, T., Frey, F.A., Garcia, M.O., Gurenko, A.A., Kamenetsky, V.S., Kerr, A.C., Krivolutskaya, N.A., Matvienkov, V.V., Nikogosian, I.K., Rocholl, A., Sigurdsson, I.A., Sushchevskaya, N.M., Teklay, M., 2007. The amount of recycled crust in sources of mantle-derived melts. Science 316, 412–417.

Sun, S., McDonough, W.F., 1989. Chemical and isotopic systematics of oceanic basalts: implications for mantle composition and processes. Geol. Soc. (Lond.) Spec. Publ. 42, 313–345.

Tamura, Y., Ishizuka, O., Stern, R.J., Shukono, H., Kawabata, H., Embley, R.W., Hirahara, Y., Chang, Q., Kimura, J.-I., Tatsumi, Y., Nunokawa, A., Bloomer, S.H., 2011. Two primary basalt magma types from Northwest Rota-1 volcano, Mariana Arc and its mantle diapir or mantle wedge plume. J. Petrol. 52, 1143–1183.

Thompson Stiegler, M., Lowe, D.R., Byerly, G.R., 2011. Fragmentation and dispersal of komatiitic pyroclasts in the 3.5–3.2 Ga Onverwacht Group, Barberton greenstone belt, South Africa. GSA Bull. 123, 1112–1126.

Ulmer, P., 2001. Partial melting in the mantle wedge—the role of H_2O in the genesis of mantle-derived 'arc-related' magmas. Phys. Earth Planet. Inter. 127, 215–232.

Van Keken, P.E., Hacker, B.R., Syracuse, E.M., Abers, G.A., 2011. Subduction factory: 4. Depth-dependent flux of H_2O from subducting slabs worldwide. J. Geophys. Res. 116, B01401. http://dx.doi.org/10.1029/2010JB007922.

Vigouroux, N., Wallace, P.J., Kent, A.J.R., 2008. Volatiles in high-K magmas from the western trans-Mexican volcanic belt: evidence for fluid fluxing and extreme enrichment of the mantle wedge by subduction processes. J. Petrol. 49, 1589–1618.

Walker, G.P.L., Croasdale, R., 1972. Characteristics of some basaltic pyroclastics. Bull. Volcanol. 35, 303–317.

Wasylenki, L.E., Baker, M.B., Kent, A.J.R., Stolper, E.M., 2003. Near-solidus melting of the shallow upper mantle: partial melting experiment on depleted peridotite. J. Petrol. 44, 1163–1191.

Wilson, R.A., 2003. Geochemistry and petrogenesis of Ordovician arc-related mafic volcanic rocks in the Popelogan inlier, northern New Brunswick. Can. J. Earth Sci. 40, 1171–1189.

Woodland, S.J., Pearson, D.G., Thirlwall, M.F., 2002. A platinum group element and Re–Os isotope investigation of siderophile element recycling in subduction zones: comparison of Grenada, Lesser Antilles arc and the Izu-Bonin arc. J. Petrol. 43, 171–198.

Yamamoto, M., 1988. Picritic primary magma and its source mantle for Oshima–Ōshima and back-arc side volcanoes, Northeast Japan arc. Contrib. Mineral. Petrol. 99, 352–359.